Computational Mechanics (2020) 66:707–722
https://doi.org/10.1007/s00466-020-01873-7

ORIGINAL PAPER

Numerical investigation of microscale dynamic contact angles of the CO_2–water–silica system using coarse-grained molecular approach

Pengyu Huang[1] · Luming Shen[1] · Yixiang Gan[1] · Federico Maggi[1] · Abbas El-Zein[1]

Received: 24 February 2020 / Accepted: 17 June 2020 / Published online: 3 July 2020

Abstract
The dynamic contact angle of a gas–liquid–solid system depends on the contact line velocity and ignoring this effect could lead to inaccurate estimations of the capillary pressures in microporous media. While most existing coarse-grained molecular dynamics (CGMD) models use one particle to represent a few molecules, we present a novel CGMD framework to model microscale CO_2/water flows in silica with each particle representing hundreds of thousands of molecules. The framework can reproduce the densities and viscosities of water and CO_2, water–CO_2 interfacial tension, and static contact angle over a wide range of pressures. The validated framework is applied to study the velocity-dependency of contact angle of the microscale CO_2–water–silica system. The results indicate that the assumption in the molecular kinetic theory that liquid–solid interaction is similar to the reversible work of adhesion between liquid and solid may not hold for CO_2–water–silica systems.

Keywords CO_2–water–silica system · Dynamic contact angle · Coarse-grained molecular dynamics · Dissipative particle dynamics · Multiphase interactions

1 Introduction

The utilization of supercritical CO_2 has gained interest in energy areas, such as CO_2 flooding for enhanced oil recovery, hydraulic fracturing, and displacement of methane from gas hydrate [1–3]. It is therefore important to understand the behaviour of CO_2/water flow in sedimentary micropores. The wettability of the system, which is usually quantified using the contact angle, is an essential factor for the studies of multiphase flow. The static contact angle is measured when there is no relative movement between the three-phase contact line and the solid surface. The dynamic contact angle is measured during the multiphase flow because the contact line is moving relative to the solid surface. The effects of pressure, temperature, and salt concentrations on the static contact angle of the CO_2–water–silica systems have been studied using experiments [4–6] and at the nanoscale using molecular dynamics (MD) simulations [7–10]. Different trends have been experimentally observed for the contact angle changes with pressure, and hence the MD method has been used to eliminate experimental uncertainties such as surface contaminations and chemical reactions [7, 11]. Recently, MD simulations have been carried out to study the effect of the contact line velocity on the dynamic contact angle, and simulation results have been found to be consistent with the molecular kinetic theory (MKT) [12]. However, to our knowledge, changes in the dynamic contact angle as a function of the contact line velocity for the CO_2–water–silica system have not been studied experimentally. The study of the dynamic wetting is important in many applications, such as the design of microfluidic devices, coating, and lubrication. The rate-dependent behaviour of the dynamic contact angle can affect the calculation of capillary pressure in porous media since the capillary pressure is calculated as a function of Young–Laplace equation [13]. Numerical simulators can offer an attractive tool to study and quantify this dependency at the microscale.

Several numerical methods have been used to study the dynamic contact angle in multiphase flow, such as MD, lattice-Boltzmann method (LBM) [14], smooth particle hydrodynamics (SPH) [15–17], computational fluid dynamics (CFD) [18], and finite element method (FEM) [19, 20].

✉ Luming Shen
luming.shen@sydney.edu.au

[1] School of Civil Engineering, The University of Sydney, Sydney, NSW 2006, Australia

In MD, the dynamic contact angle depends on molecular interactions, but the simulation is limited to the length scale of nanometres and the time scale of nano-seconds with high computational costs. A multiscale moving contact line model was developed and implemented in the framework of FEM by coupling the coarse-grained adhesive model and the macroscale hydrodynamic model [19, 20]. Indeed, the multiscale model can effectively separate the liquid and solid phases at their contact surface to avoid the singularity problem at the contact line. Nevertheless, it only models the liquid and solid phases explicitly. The problem becomes more challenging when the dynamics of the gas phase are added. LBM, SPH, and CFD can also be used to study dynamic contact angle at the microscale (at the order of a few to hundreds of microns). LBM or CFD can be coupled with the discrete element method (DEM) to consider the effect of the movement of solid particles [21, 22], but they cannot model the deformation or fracture of the solid, which could be significant in several engineering applications (e.g., hydraulic fracturing). Although SPH can theoretically model solid fracturing [23] and the dynamic contact angles of multiphase flow [16], simulating the complex interactions between multiphase flow and solid fracture at the microscale using SPH alone is still very challenging.

Coarse-grained molecular dynamics (CGMD) methods have been proposed to achieve greater length and time scales than MD by reducing the number of degrees of freedom [24, 25]. A few CGMD models for CO_2 and water have been developed as well, but most are done by mapping one molecule or a few molecules (i.e. 4 water molecules) into one CG particle with a particle size of around 0.3–0.6 nm [24–27]. A higher level of coarse-graining (mapping many molecules into one particle) is needed to model the multiphase interactions at the microscale (micrometer length and microsecond time scales). Dissipative particle dynamics (DPD) [28] and many-body dissipative particle dynamics (MDPD) [29, 30] methods were applied to model single-phase flow and liquid–vapour phases to model the liquid at the microscale by mapping many molecules (e.g. $\sim 10^7$ water molecules) into one CG particle [31, 32]. By combining the features of SPH and DPD, the smoothed dissipative particle dynamics (SDPD) method was developed to fill the gaps between the microscale (or mesoscale as described in Ref. [33]) and macroscale by Espanol and Revenga [33, 34]. The SDPD returns to a SPH method for solving the Navier–Stokes equations at the macroscale, and recovers the scale-dependent thermal fluctuations at the microscale [34]. SDPD works better than the conventional DPD for fluids since the equation of state and viscosity are input to the method. Besides, the SDPD can model the multiphase flows by implementing and modifying the methods used in SPH [35, 36]. SDPD currently cannot be applied to model the deformation or fracture of the solid, since it has mainly been developed to solve the Navier–Stokes equations at the macroscale. Modeling the deformable solid can be important in many porous media applications where the complex liquid–gas-solid interactions must be simulated explicitly. Recently, a CGMD framework has been developed to describe the liquid–vapour–solid system successfully at the microscale with the capability of capturing solid deformation and fracture [37]. However, the CG framework cannot be applied to model CO_2/water flow at the microscale since it did not consider CO_2 and the dynamic property of the liquid, such as viscosity [37], which is important in the modelling of multiphase flows. Most CG models for CO_2 use one CG particle to represent one CO_2 molecule [24, 38, 39], and there is no CG model developed by mapping large numbers of CO_2 molecules into one CG particle.

This paper develops a new CGMD framework for modelling CO_2–water–silica systems at the micrometer length and microsecond time scales. The proposed framework combines MDPD and DPD force fields, and Lennard–Jones potential function. The MDPD force field is used to describe the water–water inter-particle interaction, as in [37]. The DPD force field is used to describe the inter-particle interaction of the supercritical CO_2. The Lennard–Jones potential function is used to describe the interactions between different phases. The parameters of the particle–particle interactions will be calibrated to reproduce the experimentally measured densities and viscosities of CO_2 and water, the interfacial tension between water and CO_2, and the static contact angle at different pressures ranging from 10 to 20 MPa. The proposed framework will then be used to model and study the dynamic contact angle as a function of velocity for the microscale CO_2–water–silica system under high pressure (10–20 MPa) and high temperature (333.15 K) conditions. The dynamic contact angles at different velocities and capillary numbers $Ca = \mu v/\gamma$ will be calculated by modelling the piston-induced flow at three different water pressures, where v is the velocity of the moving contact line, μ is the viscosity of the liquid, and γ is the interfacial tension between the liquid and gas phases. The calculated dynamic contact angle at different contact line velocity will be compared with previous MD results [12]. A sensitivity analysis of the interaction between solid and water and the interaction between solid and CO_2 will be carried out as well to study how dynamic contact angle as a function of contact line velocity is affected by different solid–fluid interactions.

2 Computational methods

2.1 Potential functions for inter-particle interactions

The fluid and interfacial properties in the CG approach depend on the particle–particle interactions, which govern the motion of particles in the simulated system. Here, the interaction between water particles is described by the MDPD force field, as per [37]. DPD forces field is used to describe the interaction between supercritical CO_2 particles because the surface tension of the supercritical CO_2 in liquid–vapour equilibrium is extremely small (the surface tension is 0.054 mN/m at a temperature of 303.15 K and approaches to zero as the temperature increases [40]) and can be neglected. The interactions between different phases are described by the Lennard–Jones (LJ) potential function. The solid particles are fixed here for simplicity, but the interactions between them can be considered and calibrated against the tensile strength and Young's modulus of the fused silica if needed [37]. The calculated dynamic contact angle will not be affected by using fixed solid particles instead of mobile solid particles since our preliminary results have shown that the displacements of the solid particles are very small under the applied loading conditions.

For the DPD and MDPD forces, only the conservative part is used in this study. The dissipative and random forces, which work together as a DPD thermostat, are not considered here and are replaced by the Nosé–Hoover chains thermostat [41, 42]. For DPD particles, the DPD thermostat is commonly used to adjust the viscosity of the fluid for the dynamics of CG particles [28]. Alternatively, Nosé–Hoover thermostat can be used in CGMD [27]. In our CG model, the thermodynamic properties of fluids are mainly controlled by the conservative forces (or the pairwise potential functions). Hence the Nosé–Hoover chains thermostat is used as a weakly-coupled thermostat for modelling the system at a targeted temperature. Besides, Nosé–Hoover chains thermostat can be easily applied to solid particles if modelling the deformation or fracture of the solid is desired at the same time, as demonstrated in [37]. For MDPD, the conservative force is given by

$$\mathbf{F}_{\mathrm{ij}}^{\mathrm{MDPD}} = Aw_c\left(r_{ij}\right)\mathbf{e}_{ij} + B\left(\rho_i + \rho_j\right)w_d\left(r_{ij}\right)\mathbf{e}_{ij}, \tag{1}$$

where A and B are parameters of the attractive and repulsive forces (A is negative, and B is positive), respectively; r_{ij} is the distance between the particles i and j; $\mathbf{e}_{ij}$ is the unit vector pointing from particle j to particle i; $w_{\mathrm{c}}(r_{ij})$ and $w_{\mathrm{d}}(r_{ij})$ are the weight functions defined as:

$$w_c\left(r_{ij}\right) = \begin{cases} 1 - \frac{r_{ij}}{r_c} & r_{ij} \le r_c \\ 0 & r_{ij} > r_c \end{cases}, \tag{2}$$

$$w_d\left(r_{ij}\right) = \begin{cases} 1 - \frac{r_{ij}}{r_d} & r_{ij} \le r_d \\ 0 & r_{ij} > r_d \end{cases}, \tag{3}$$

where r_{c} and r_{d} are the cut-off distances for the attractive and repulsive forces, respectively. r_{c} is larger than r_d in MDPD to recover the attractive force at the liquid–vapour interface. The weighted local density of particle i, ρ_i [Eq. (1)], is calculated as the sum of the weight function w_{ρ} of its neighbour particles within the cut-off radius r_{d}:

$$\rho_i = \sum_{j \neq i} w_\rho = \sum_{j \neq i} \frac{15}{2\pi r_d^3}\left(1 - \frac{r_{ij}}{r_d}\right)^2, \quad r_{ij} \le r_d. \tag{4}$$

For conventional DPD the conservative forces are given by:

$$\mathbf{F}_{ij}^{DPD} = Aw_c\left(r_{ij}\right)\mathbf{e}_{ij}, \tag{5}$$

where A is the parameter of the repulsive force and is positive.

The LJ potential energy $u_{\alpha\beta}$, which describes the interactions between two particles from different phases separated by a distance $r_{\alpha\beta}$, is given by:

$$u_{\alpha\beta} = \begin{cases} 4\varepsilon_{\alpha\beta}\left[\left(\frac{\sigma_{\alpha\beta}}{r_{\alpha\beta}}\right)^{12} - \left(\frac{\sigma_{\alpha\beta}}{r_{\alpha\beta}}\right)^{6}\right] & r_{\alpha\beta} < r_{\alpha\beta,cut} \\ 0 & r_{\alpha\beta} \ge r_{\alpha\beta,cut} \end{cases}, \tag{6}$$

where $\varepsilon_{\alpha\beta}$ and $\sigma_{\alpha\beta}$ are the depth of the potential well and the distance at zero potential energy, respectively. The subscript $\alpha\beta$ indicates different types of interactions: cw for CO_2–water interactions, sc for silica–CO_2 interactions, and sw for silica–water interactions. $r_{\alpha\beta,\,\mathrm{cut}}$ is the cut-off radius, which is set as 2.5 in dimensionless units for all cases.

2.2 Conversion between dimensionless to dimensional systems

Simulations are run in dimensionless units. The dimensionless units of mass m^*, energy E^*, and length L^* are set as unity and defined as:

$$m^* = \frac{m}{m_{water}} \tag{7}$$

$$L^* = \frac{L}{r_c} \tag{8}$$

$$E^* = \frac{E}{\varepsilon}, \tag{9}$$

where m_{water} is the mass of a water particle, r_c is the cut-off distance for the attractive force in the MDPD model for water, and ε is the unit of energy for the simulated system. Here, the dimensionless variables are written with the asterisk.

The next step is to determine the reference values: m_{water}, r_c, and ε. As the reservoirs often experience high-temperature and high-pressure conditions, a model of CO_2–water–silica system at a high-pressure between $P = 10$ MPa and 20 MPa at $T = 333.15$ K will be developed. CO_2 is at its supercritical state under such high pressure and high temperature since the critical pressure of CO_2 at $T = 333.15$ K is around 7.4 MPa [40]. ε, r_c, and m_{water} can be calculated by matching the real pressure P, the interfacial tension between CO_2 and water γ, and the density of the water ρ_{water} at 15 MPa and 333.15 K with their dimensionless values below, by:

$$P^* = P\left(\frac{r_c^3}{\varepsilon}\right), \tag{10}$$

$$\gamma^* = \gamma\left(\frac{r_c^2}{\varepsilon}\right), \tag{11}$$

$$\rho^*_{water} = \rho_{water}\left(\frac{r_c^3}{m_{water}}\right). \tag{12}$$

After the rearrangement of Eqs. (10) to (12), ε, r_c, and m_{water}, can be expressed as:

$$\varepsilon = \left(\frac{\gamma}{\gamma^*}\right)^3\left(\frac{P^*}{P}\right)^2, \tag{13}$$

$$r_c = \left(\frac{\gamma}{\gamma^*}\right)\left(\frac{P^*}{P}\right), \tag{14}$$

$$m_{water} = \frac{\rho_{water}}{\rho^*_{water}}\left(\frac{\gamma}{\gamma^*}\right)^3\left(\frac{P^*}{P}\right)^3 = \frac{\rho_{water}}{\rho^*_{water}} r_c^3. \tag{15}$$

Here, $\rho_{\text{water}} = 989.6$ kg/m^3 and $\gamma = 0.0305$ N/m are used [40, 43]. It is noted that the experimental value of γ was obtained at 333.5 K instead of the 333.15 K in the simulation. Here, it is assumed that the simulated CG system at $T^* = 1$ is equivalent to the system at the real temperature $T = 333.15$ K, as the temperature is not varied in this study. $P^* = 120$ is assumed to be the pressure at 15 MPa as elaborated next. It can be seen from Eq. (14) that it is better to choose a larger P^* value so that a larger physical scale of the coarse-grained particles can be achieved when other variables are kept unchanged. However, if the selected P^* value is too large, the liquid phase may become solid. Using $P^* = 120$ will allow us to study the flow in a microchannel with a channel size of around 1 μm. To link the dimensionless unit of viscosity to its physical unit, the definition of the time unit τ is also required. Usually, the dimensional time unit is calculated as $\tau = r_c(m_{\text{water}}/\varepsilon)^{1/2}$, and the dimensionless time unit is defined as $\tau^* = \tau\,(\varepsilon/m_{\text{water}})^{1/2}/r_c$. The time unit has been scaled to match the experimental diffusion constant of water for DPD particles in [44, 45]. In this work, since the viscosity is one of the targeted properties, the time unit τ is calculated to match the experimental water viscosity η_{water} at 15 MPa and 333.15 K using the following equation:

$$\tau = \frac{\eta_{water} r_c^3}{\eta^*_{water}\varepsilon}, \tag{16}$$

where η^*_{water} is the viscosity calculated from the simulations at $P^* = 120$ and $T^* = 1$.

2.3 Calibration of the DPD/MDPD system

Equations (13)–(16) can link the dimensionless system to the dimensional system at $P = 15$ MPa and $T = 333.15$ K by calculating the fundamental values ε, r_c, m_{water}, and τ for a certain set of parameters. Afterwards, the parameters of the particle–particle interactions can be calibrated accordingly to reproduce the experimental values of the density, interfacial tension, viscosity for a wide range of pressure, i.e., 10 MPa to 20 MPa. For water, the MDPD parameters of $A^* = -40$, $B^* = 50$, $r_d^* = 0.75$ and $r_c^* = 1$ are chosen following our previous study [37]. The parameters of the MDPD (water particles) and DPD (CO_2 particles) are only calibrated against the experimental viscosity ratio of water to CO_2 at $P = 15$ MPa and $T = 333.15$ K, i.e., 10:1, because it is found from the simulations that the compressibility of both CO_2 and water under high pressures cannot change much by adjusting the force parameters. Although the CO_2 and water models are not calibrated against their compressibility, it will be shown later in Sect. 3.1 that the resulting parameters recover the densities of CO_2 and water well, over a large range of pressure. However, some discrepancies in the CO_2 density are observed at $P \le 14$ MPa.

The calibration of the DPD parameter in this work is conducted as follows (see flowchart in Fig. 1). Given the MDPD parameters ($A^* = -40$, $B^* = 50$, $r_d^* = 0.75$ and $r_c^* = 1$), ρ^*_{water} and η^*_{water} can be calculated at $P^* = 120$ and $T^* = 1$ from the simulations (see Appendices 1 and 2 for the calculations of the density and the viscosity). Afterwards, for each set of DPD parameters, the dimensionless number particle density $\rho^*_{\text{CO2, n}}$ can be calculated at $P^* = 120$ and $T^* = 1$.

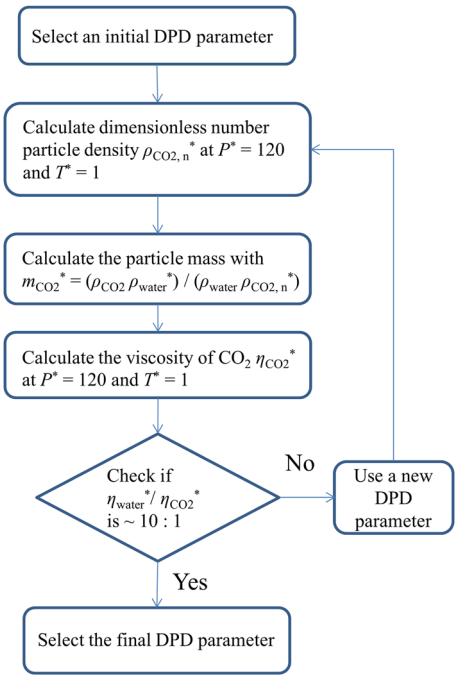

Fig. 1 Flow chart of calibrating the DPD parameter against the viscosity ratio $\eta^*_{water}/\eta^*_{CO2}$, given a set of MDPD parameters

Then, m^*_{CO2} can be calculated as $m^*_{CO2} = (\rho_{CO2}\,\rho^*_{water})/(\rho_{water}\,\rho^*_{CO2,n})$, which can be derived from Eqs. (7) and (15). Next, the viscosities of CO_2, η^*_{CO2}, can be calculated at $P^* = 120$ and $T^* = 1$. In the end, the DPD parameters $A^* = 70$ is chosen, with a viscosity of 1.54, resulting in a viscosity ratio of $\eta^*_{water}/\eta^*_{CO2} = 9.45$: 1, at $P^* = 120$ and $T^* = 1$. The viscosities of water and CO_2 at a wide range of pressure are also calculated accordingly. After the calibration of the MDPD and DPD parameters, the parameters of LJ potential function for the particle–particle interactions between CO_2 and water can be calibrated with a trial and error method against experimental interfacial tension for the pressure varying from 10 MPa to 20 MPa (see Appendix 3 for the calculation of the interfacial tension).

Next, the parameters of the particle–particle interactions of CO_2–silica and water–silica are calibrated against the static contact angle for the CO_2–water–silica as a function of pressure. Two factors are considered in the calibration process. The first factor is that the silica surface needs to be modelled as hydrophilic. This is because amorphous silica surfaces in aqueous environments have an area density of (Si–O–H) group around 4.6–4.9 nm^{-2}, which leads to a complete wetting in a water–vapour (vacuum)–silica system [12]. A water bridge method will be performed to confirm if the silica surface is hydrophilic (see the detailed calculations in Appendix 4). The other factor is that the simulated contact angle over a broad range of pressures should be consistent with the literature. Since there are significant

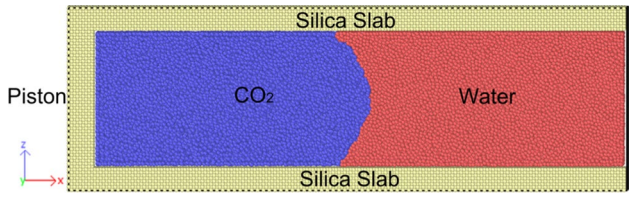

Fig. 2 The simulated system obtained after equilibration at $P = 14.4$ MPa and $T = 333.15$ K using visualisation software OVITO [52]

discrepancies in the measured contact angle as a function of pressure in the reported experiments, it is assumed that the resulting static contact angle of the CO_2–water–silica system should be similar to our previous MD simulations [12] and does not change with pressure at our studied pressure range. This pressure dependence is also consistent with some experimental studies [46, 47]. In addition, a range of static contact angles is modelled by changing the interaction energy between silica and water particles and between silica and CO_2 particles.

2.4 Static and dynamic contact angle simulations

All simulations in this work are computed using LAMMPS code [48]. The implementation of MDPD in LAMMPS is done by using the embedded atom method (EAM) potentials (see [37] for details). The EAM tabulated files are generated by the "atsim.potentials" code [49]. The Nosé–Hoover chains thermostat is used for the system running in a constant-particle-number, constant-volume, constant-temperature (*NVT*) ensemble unless otherwise stated. The isothermal–isobaric ensemble (constant-particle-number, constant-pressure, constant-temperature *NPT* ensemble) is achieved with both a Nosé–Hoover chains thermostat and a Parrinello–Rahman barostat [41, 42, 50, 51]. The damping parameters of the thermostat and the barostat are 100 time steps and 1000 time steps, respectively.

To calculate the static and dynamic contact angles of the CO_2–water–silica system, a periodic simulation box containing CO_2 and water within two silica slabs is created (see Fig. 2). The size of the simulation box size is $L_x = 2.71$ μm, $L_y = 0.371$ μm, and $L_z = 0.964$ μm. The channel height is $D_z = 0.741$ μm. A piston is placed at the left end of the simulation box (Fig. 2). The solid slabs and the piston are considered as the silica and are constructed using a face-centered cubic (FCC) lattice structure with a particle density of 6 per unit volume V^*, same as the particle density of water at $P = 15$ MPa. The thickness of the slabs and pistons is chosen to be greater than the cut-off radius of the LJ potential function. The interactions between the slabs and the piston are turned off in the simulations. Initially, the equilibrated water and CO_2 phases are placed in between the slabs. To prepare the equilibrated

water and CO_2 phases, a water box and a CO_2 box are obtained from bulk water and CO_2 phases in the equilibrated water–CO_2 interface simulations, respectively. Each box has a size of $L_x = L_z = 0.354$ μm and $L_y = 0.371$ μm. Each box is further replicated four times in the x-direction and two times in the z-direction and then is equilibrated for 100,000 time steps at an *NVT* ensemble. Finally, the equilibrated water and CO_2 phases are placed between the slabs in the simulation box. Sufficient gaps between different phases are left to avoid the undesired large forces when placing the water and CO_2 particles.

The initial velocities of the water and CO_2 particles of the system are drawn randomly from the Gaussian distribution at a given temperature. An energy minimisation process is applied to water and CO_2 particles to avoid large overlaps between particles. Then, only water particles move under a Langevin thermostat for 10,000 time steps for a quick relaxation of the water, while keeping other particles fixed. Similarly, a quick relaxation for CO_2 is carried out with the same procedure for another 10,000 time steps. The relaxation processes can prevent the initial interface shape from changing significantly because a large amount of energy can initially be generated at the interface. The CO_2 and water particles are then further relaxed with a Langevin thermostat for 100,000 time steps to reach thermal equilibrium. The thermostat is then switched to the Nosé–Hoover chains thermostat for the rest of the run in an *NVT* ensemble for 2,000,000 time steps. The first 1,000,000 time steps are considered as the equilibrium run, and the last 1,000,000 time steps are considered as a production run. In simulations at high pressure (~20 MPa), it takes a long time to reach the equilibrium state (3,000,000 time steps), and the following 1,000,000 time steps (production run) are used for the calculation of the contact angles. The calculation of contact angle is reported in Appendix 5. A time step size $\Delta\tau^* = 0.0025\tau^*$ is used to ensure that the integration of the particle motion in the equilibrated system is stable.

Five different pressures are considered in the static contact angle simulations where the piston does not move. For the calculations of dynamic contact angle, the simulations start from the equilibrated system obtained from the static contact angle simulations, with a moving piston at different constant velocities. The temperature used in the Nosé–Hoover chains thermostat does not include the contribution from the particle velocities in the flow direction (the x-direction) during the dynamic contact angle simulations. At the beginning of the simulations, the velocity of the piston increases linearly from zero to the targeted velocity within 100,000 time steps to avoid the potential shock wave due to the sudden increase of the piston velocity. Then, the simulations are run for 2,000,000 time steps, with the equilibrium run of the first 1,000,000 time steps and the production run of the last 1,000,000 time steps. The data from the production run is used to calculate dynamic contact angles. Initially, three different channel sizes are simulated at a specific pressure (i.e. water pressure of ~ 14 MPa after equilibrium): 0.742, 1.11, and 1.48 μm, and the size of the simulation box is scaled accordingly, to study the finite-size effect of the simulations. Afterwards, the dynamic contact angle simulations are computed at three different water pressures. Finally, contact angle simulations are performed with different silica–CO_2 and silica–water interactions to study the effects of solid–gas and solid–liquid interactions on the rate-dependent behaviour of the dynamic contact angle.

3 Results and discussion

The calibrated parameters of the interactions between the particles from the same and different phases in dimensionless units are given in Tables 1 and 2, respectively. The calculated fundamental values are listed as: mass unit $m_{water} = 7.29 \times 10^{-21}$ kg (equivalent to mapping 2.4×10^5 water molecules into one CG particle of water), energy unit $\varepsilon = 5.53 \times 10^{-18}$ J, length unit $r_c = 0.0354$ μm, and time unit $\tau = 0.257$ ns. The mass of a CO_2 particle is 6.5×10^{-21} kg, which means 8.9×10^4 CO_2 molecules are mapped into one CG particle of CO_2. The average particle sizes for water and CO_2 can be calculated from the particle density as 0.019 μm and 0.022 μm, respectively, at $P = 15$ MPa and $T = 333.15$ K. These particle sizes and the time unit ensure that the proposed CGMD framework can model the CO_2/water flows in silica at a length scale of micrometers and a time scale of microseconds. The fundamental values and parameters of the fluid properties are also listed in Table 3, with the

Table 2 Interaction parameters between two unlike particles

Particle–particle interactions	Force field	$\varepsilon^*_{\alpha\beta}$	$\sigma^*_{\alpha\beta}$
Water/CO_2	LJ	0.07	0.8
Water/solid	LJ	0.5	0.85
CO_2/solid	LJ	0.08	1.03

Table 1 Interaction parameters for water and CO_2 particles

Particle–particle interactions	m^*	Force field	A^*	B^*	r^*_c	r^*_d
Water/water	1	MDPD	−40	50	1	0.75
CO_2/CO_2	0.891	DPD	70	–	1	–

equations for calculating fundamental values and the relations between the dimensional values and dimensionless ones.

3.1 Fluid properties

The simulated density and viscosity of CO_2 and water, and the CO_2–water interfacial tension using the parameters listed in Tables 1 and 2 are reported in this section. Figure 3a shows the simulated densities of CO_2 and water compared with the experimental data obtained from the National Institute of Standards and Technology Chemistry Webbook (NIST database) [40]. The simulated density of water slightly deviates from the experimental values at $P = 10$ MPa and 20 MPa with differences less than 5% (Fig. 3a). The simulated density of the CO_2 matches the experimental data for $P \geq 14$ MPa, but there is a large discrepancy between the simulation and the experiment for P from 10 MPa to 14 MPa. It can be seen that the CO_2 density changes with pressure for P between 10 MPa and 14 MPa at a rate greater than the density change rate for $P \geq 14$ MPa. The applied DPD force field for modelling the CO_2 cannot replicate this feature and hence causes the discrepancy. Since the empirical equation of dynamic contact angles is usually expressed as a function of capillary number Ca, which is a function of the contact line velocity, the viscosity of the liquid, and the interfacial tension between the liquid and gas phases [53, 54], the effect of fluid density is not taken into account in this case. Therefore, it is reasonable to assume that the discrepancies in the CO_2 density at low pressures may not be an important factor in the study of dynamic wetting.

Figure 3b shows the simulated and experimentally measured CO_2–water interfacial tension under pressure P ranging from 10 MPa to 20 MPa. The statistical errors of the interfacial tension are calculated by estimating the statistical inefficiency. Bachu and Bennion's experimental results [55] (at 333.15 K) and Georgiadis et al.'s results [43] (at 333.5 K) are consistent for the interfacial tension under various pressures at a temperature around 333 K, but are larger than those of Bikkina et al. [56] (at 333.15 K) for P > ~ 14 MPa, as shown in Fig. 3b. Bikkina et al. attributed this discrepancy to the deviations of the saturated phase densities from the pure compound densities at the high pressure and low-temperature range, since Georgiadis et al. used the pure compound densities (obtained from National Institute of Standards and Technology Chemistry Webbook) instead of the measured densities (saturated densities) in the calculation of the interfacial tension value [56]. However, we found that Bachu and Bennion also used the saturated densities that were measured from the experiments in their calculation of the interfacial tension and still found values compatible with those of Georgiadis et al. [55]. Hence, the deviations in the experimental results of Bikkina et al. could be due to other, unspecified experimental factors. In this work, the parameters of the LJ potential function between CO_2 and water phases are calibrated against the trend of the experimental data obtained from the work of Georgiadis et al. [43]. As a result, our simulated interfacial tension results match well with their data and those of Bachu and Bennion [55].

Figure 3c compares the simulated viscosities of CO_2 and water by our CG model and experimentally measured viscosities obtained from the NIST database [40]. For the calculation of the viscosity, five simulations are carried out for each case, and then the average and standard deviations are calculated. Simulated CO_2 and water viscosities match well with experimental data, although the simulated CO_2

Table 3 The fundamental units and the fluid properties of the simulated systems and the relations to their dimensionless values at $P = 15$ MPa and $T = 333.15$ K

Type of parameters	Parameters	Calculations of the parameters	Relation to the dimensionless value	Physical values
Fundamental units	ε	$\left(\frac{\gamma}{\gamma^*}\right)^3\left(\frac{P^*}{P}\right)^2$	$\varepsilon\,\varepsilon^*$	5.53×10^{-18} J
	r_c	$\left(\frac{\gamma}{\gamma^*}\right)\left(\frac{P^*}{P}\right)$	$r_c\,r_c^*$	0.0354 μm
	m_{water}	$\frac{\rho_{water}}{\rho^*_{water}}r_c^3$	$m_{water}m^*_{water}$	7.29×10^{-21} kg
	m_{CO2}	$\frac{\rho_{CO2}}{\rho^*_{CO2}}r_c^3$	$m_{water}m^*_{CO2}$	6.5×10^{-21} kg
	τ	$\tau = \frac{\eta_{water}r_c^3}{\eta^*_{water}\varepsilon}$,	$0.2r_c(m_{water}/\varepsilon)^{1/2}\tau^*$ [a]	0.257 ns
Fluid properties	ρ_{water}	–	$m_{water}\rho^*_{water}/r_c^3$	989.7 kg/m^3
	ρ_{CO2}	–	$m_{CO2}\rho^*_{CO2}/r_c^3$	604.07 kg/m^3
	η_{water}	–	$\varepsilon\tau\,\eta^*_{water}/r_c^3$	470.3 μPa s
	η_{CO2}	–	$\varepsilon\tau\,\eta^*_{CO2}/r_c^3$	49.81 μPa s
	γ	–	$\varepsilon\gamma^*/r_c^2$	30.5 mN/m

The calculations of the fundamental units [using Eqs. (13)–(16)] are also listed

[a]The factor of 0.2 is used as the time unit is calculated by matching the simulation and experimental values of the viscosity in the CG system

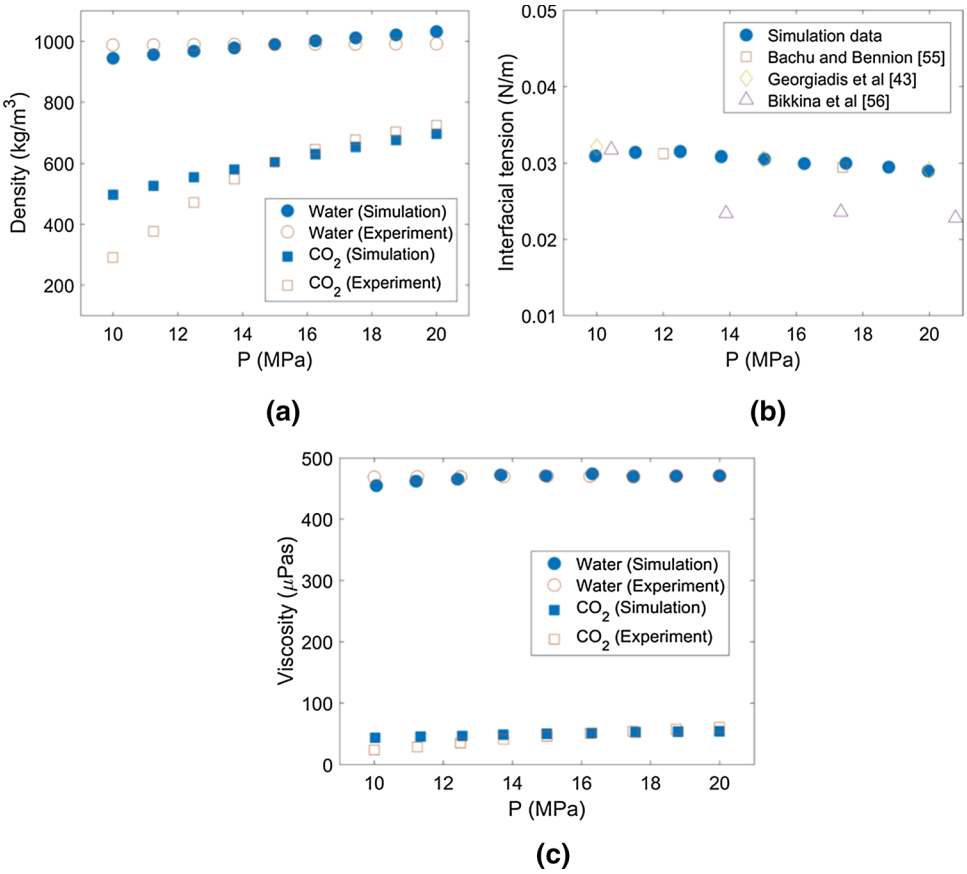

Fig. 3 Simulated and experimentally measured densities (**a**), interfacial tension between CO_2 and water (**b**), and viscosities (**c**) against pressure for water and CO_2 [40, 43, 55, 56]. The standard deviations of the calculated density for the equilibrated system are within 0.2% for CO_2 and within 0.1% for water, which are calculated from the instantaneous densities obtained at every 20 time steps. The error bars of the simulated interfacial tension (**b**) and the simulated viscosities (**c**) are smaller than the size of the markers and are not shown

viscosity is higher than the experimental value at pressures below 12.5 MPa.

As mentioned earlier, it is crucial to recover the experimental values of viscosity and interfacial tension for the study of the dynamic contact angle at the moving contact line. It has been demonstrated here that the proposed CG framework is capable of recovering the experimental interfacial tension between CO_2 and water, and the density and viscosity of CO_2 and water over a broad range of pressures.

3.2 Static contact angle

A water bridge simulation has been carried out to ensure a water-wet surface of the solid using the parameters given in Tables 1 and 2. Figure 4 shows a snapshot of the water bridge simulation at equilibrium. A complete wetting has been observed from the simulation, which suggests that the silica surface is hydrophilic for the water–vapour (vacuum)–silica system. It should be noted that the simulated density of the water would be lower than the real water density, as the calibration of the parameters of the water model is not performed against the experimental data at the low-pressure conditions for the water–vapour system. Although the particle density of water model would be higher in the high-pressure range (from 10 to 20 MPa) than that of the water–vapour system, it is expected that the higher particle density of water would result in stronger silica–water interactions. Therefore, the silica surface would still be hydrophilic at high-pressure conditions.

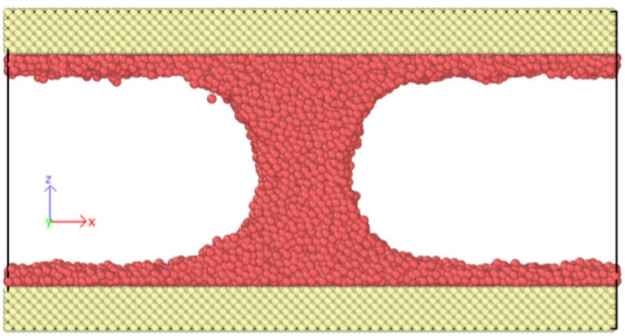

Fig. 4 A snapshot of the liquid bridge simulation at the equilibrium. The water particles are in red

Figure 5 compares the simulated water static contact angle θ_w in the CO_2–water–silica system using CG models at the microscale with our previous full-atom MD results at the nanoscale [12] and a few experimental works [5, 46, 47, 57]. The simulated CO_2 pressure values using CG models are determined from the pressure of the simulated

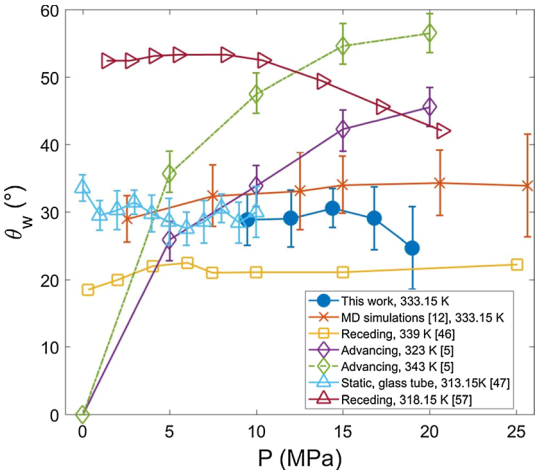

Fig. 5 The simulated water contact angle in the CO_2–water–silica system at different pressures in comparison with our previous full-atom MD results [12] and the experimental measurements from [5, 46, 47, 57] up to around $P = 25$ MPa. The data from [5, 46, 47, 57] are estimated from their figures using an online tool WebPlotDigitizer [58]. The error bars of the data from [47] are estimated from the upper error bars, as some lower error bars are too difficult to obtain

bulk CO_2 phase at the equilibrium state. The CG simulations show that there is no significant dependence of pressure on the static water contact angle for $P > 9.4$ MPa, which is consistent with our previous full-atom MD results [12]. The static contact angle values of CG simulations are similar to those of the full-atom MD simulations, but the static contact angle at $P = 19$ MPa is smaller than results from the full-atom MD simulations. Large discrepancies of the experimental contact angles as a function of pressure are found in the literature. The receding contact angle measured by Farokhpoor et al. [46] showed that there was only small dependence of pressure in the range below the CO_2 phase transition pressure, while the dependence of contact angle on pressure was not observed in the high-pressure range. Recently, Li et al. [47] studied the static contact angle for the water and CO_2 inside a micron-sized glass tube using the X-ray technique. The results of Li et al. showed no significant changes in the static contact angle with the pressure at $T = 313.15$ K, as shown in Fig. 5. However, some studies have shown the static contact angle changes with the pressure. For example, the experimental results of Sarmadivaleh et al. [5] showed that the advancing contact angle still increased with pressure for $P > 10$ MPa, although the increase rate was reduced at higher pressure. Bikkina et al. [57] even found a decrease in contact angles at the high-pressure range. Li et al. attributed the discrepancies in the experimental results to the different surface charges on the tested substrate surfaces [47]. Other possible factors could be surface contamination [11] and different experimental techniques.

3.3 Dynamic contact angle

The effect of channel size is first studied to avoid finite-size effects in the simulations. The resulting dynamic contact angles θ as a function of the contact line velocity v are shown in Fig. 6. The contact angle θ now is measured from the CO_2 phase since CO_2 is the advancing fluid. The water pressures of the three simulations are around 14 MPa after equilibrium. The resulting dynamic contact angles are statistically the same within the studied range of channel sizes. Therefore, the channel height of 0.742 μm is used for all other simulations.

The dynamic contact angle θ as a function of v for the simulated CO_2–water–silica system at three different water pressures P_{water} is shown in Fig. 7a. The water pressures are calculated from the bulk water phase. The difference between bulk CO_2 and water pressures is within 0.1 MPa. Figure 7a shows that θ increases with increasing v for all three pressure cases, but the contact angles calculated at $P_{water} = 18.9$ MPa seem to be slightly larger than those calculated at the other two pressures. Theoretically, the unbalanced interfacial force $\gamma(\cos\theta_s - \cos\theta)$ at different contact line velocities v is the driving force causing the changes in dynamic contact angle at the moving contact line, where θ_s is the static CO_2 contact angle. Therefore, it is worth plotting $(\cos\theta_s - \cos\theta)$ against v (Fig. 7b) if the γ is constant or does not change much at the three pressure cases. The results of the three CG simulations collapse into one consistent trend, which indicates that there is no significant effect of the hydrostatic pressure of fluids on how the value of $(\cos\theta_s - \cos\theta)$ changes with v in our model.

In Fig. 8 $(\cos\theta_s - \cos\theta)$ against the capillary number Ca is also plotted to consider the effects of interfacial tension and viscosity of water and compare the CG results with previous full-atom MD results obtained at a water pressure of 10.6 MPa with a channel height of 6.57 nm [12]. To estimate Ca at a specific pressure, the water viscosity and interfacial tension between CO_2 and water at the specific water pressure

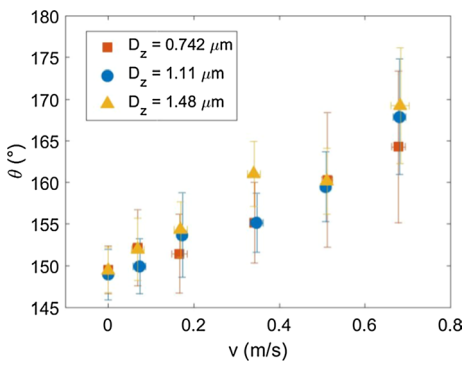

Fig. 6 CO_2 contact angle against the contact line velocity with different channel sizes at a water pressure of around 14 MPa

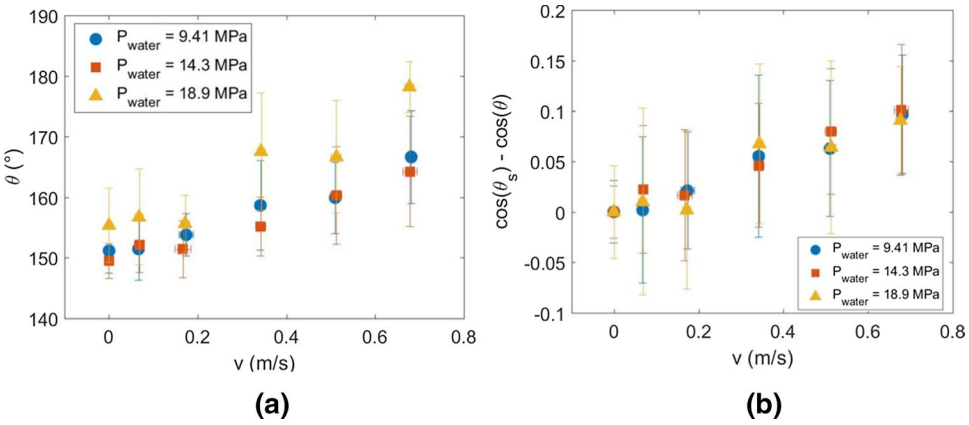

Fig. 7 **a** CO_2 contact angle against the contact line velocity, and **b** the difference between cosines of the static and dynamic contact angles versus the contact line velocity at different pressures

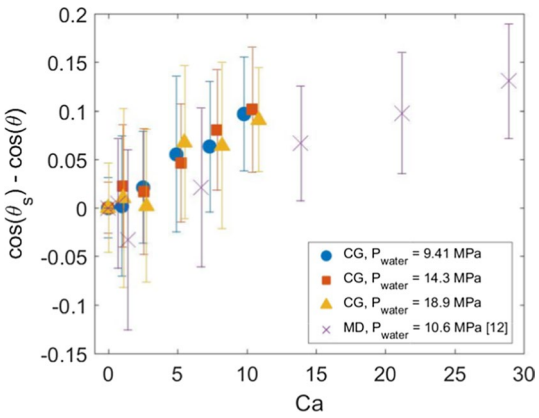

Fig. 8 The difference between cosines of the static and dynamic contact angle against the capillary number at different pressures and the relevant full-atom MD results [12]

is calculated. A third-order polynomial function is used to fit the simulated water viscosity against the pressure with $R^2 = 0.94$, and a second-order polynomial function is used to fit the simulated interfacial tension value against the pressure with $R^2 = 0.92$. Again, all three CG results obtained at different pressures follow a similar trend. It can be seen that the value of $(\cos\theta_s - \cos\theta)$ of both CG models and full-atom MD models increases at a similar rate with Ca, which means that the relationship between the unbalanced interfacial force $\gamma(\cos\theta_s - \cos\theta)$ and v of our CG model is similar to that of a full-atom MD model, given that the viscosity of water does not change much during all the simulated thermostat states (Fig. 3c). There are some discrepancies between MD and the CG results. The discrepancies may be attributed to the fact that the CG model is a simplified model of the full-atom MD. Besides, since the channel size in the full-atom MD simulations is at the nanoscale, according to the Young–Laplace equation, the capillary pressure difference between the CO_2 and water is significantly larger at the nanoscale than the pressure at the microscale, i.e. ~ 10 MPa, while the pressure difference between CO_2 and water in the CG simulations is small, i.e. ~ 0.1 MPa. The difference in fluid pressure can lead to different fluid properties and hence may also affect the behaviour of dynamic contact angles.

Although it is reasonable to assume that the static contact angle of CO_2–water–silica system is similar to the value calculated at the full-atom MD simulation, other static contact angles of CO_2–water–silica system were found in the experiments (see Fig. 5). Therefore, the effect of static contact angles on the behaviour of the dynamic contact angle is also investigated as a sensitivity analysis. Different static contact angles can be simulated by adjusting the interfacial energy between water and silica, or the interfacial energy between CO_2 and silica. Figure 9a shows the resulting dynamic contact angles when starting from different static contact angle by changing the energy parameter of the LJ potential function between silica and water particles ε_{sw}. The water pressures for all the cases are around 14.3 MPa, and hence all the cases should have similar interfacial tension and viscosity of the fluids. The rate of increase of the contact angle is generally larger, with greater static CO_2 contact angle θ_s. Furthermore, Fig. 9b plots $(\cos\theta_s - \cos\theta)$ against v. It can be seen from Fig. 9b that the larger ε_{sw} can result in a slightly larger increase rate of $(\cos\theta_s - \cos\theta)$, which has been observed in the molecular dynamics simulations previously and can be explained by molecular kinetic theory (MKT) [59, 60]. The MKT considers the dynamic contact angle at different contact line velocities as the dissipation processes of the liquid at the molecular scale. In MKT, the relationship between the contact line velocity v and the unbalanced interfacial force $\gamma(\cos\theta_s - \cos\theta)$ is expressed as [60]:

$$v = 2K_o\lambda \sinh\left(\frac{\gamma\left(cos\theta_s - cos\theta\right)}{2nk_bT}\right), \tag{17}$$

where K_o is the average jump frequency, λ is the average jump distance, T is the temperature, k_b is the Boltzmann's constant, and n is the area density of the adsorption sites on

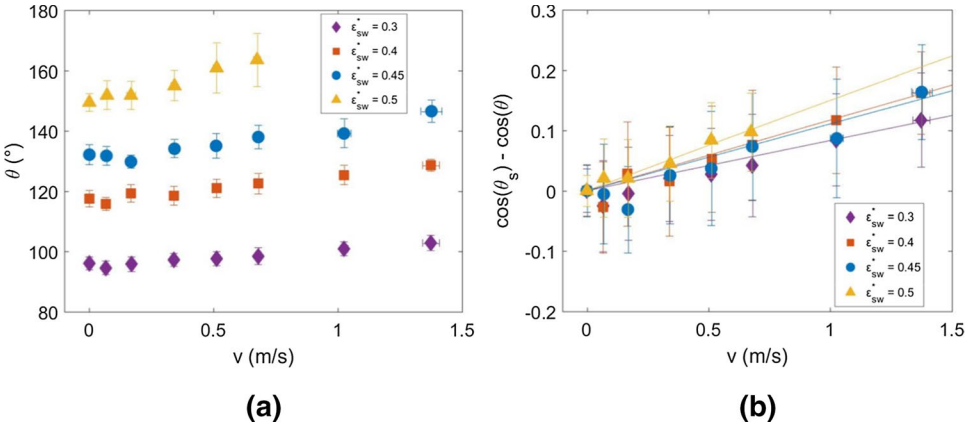

Fig. 9 **a** CO_2 contact angle against the contact line velocity, and **b** the difference between cosines of the static and dynamic contact angles against the contact line velocity with different static contact angles by changing the energy parameter for water and solid interactions. The solid lines are the fittings of Eq. (17)

the solid surface. For the derivation of Eq. (17), please refer to [60]. It has also been shown that the jump frequency K_o for the liquid–gas–solid system can be expressed as a function of the specific activation free energy of wetting per unit area Δg_w:

$$K_o = \frac{k_b T}{h} \exp\left(-\frac{\Delta g_w}{n k_b T}\right), \tag{18}$$

where h is the Plank constant. It was also suggested in the refined version of the MKT that $\Delta g_w = \Delta g_s + \Delta g_{vis}$, where Δg_s is the contribution from interactions between liquid and solid molecules, and Δg_{vis} is the contribution from the viscous interactions between liquid molecules [60]. Δg_{vis} can be related to the viscosity of liquid from the Eyring's absolute reaction rate theory: $\Delta g_{vis} = n k_b T \ln(\eta_l V_l / h)$, where η_l is the viscosity of the liquid and V_l is the molecular flow volume of the liquid [60, 61]. Hence, K_o can be expressed as:

$$K_o = \frac{k_b T}{\eta_l V_l} \exp\left(-\frac{\Delta g_s}{n k_b T}\right), \tag{19}$$

It has been suggested that Δg_s can be related to the reversible work of adhesion between the liquid and the solid W_a with the approximation [60]:

$$\Delta g_s \sim W_a = \gamma\left(1 + \cos\theta_{l,s}\right), \tag{20}$$

where $\theta_{l,s}$ is the static contact angle measured from the liquid phase, i.e. $\theta_{l,s} = 180 - \theta_s$. Hence, K_o can be expressed as:

$$K_o = \frac{k_b T}{\eta_l V_l} \exp\left(-\frac{\gamma\left(1 + cos\theta_{l,s}\right)}{n k_b T}\right). \tag{21}$$

To quantify the effect of liquid–solid interaction on the jump frequency K_o, Eq. (17) can be used to fit the simulation results with different water–solid interaction energies. Here, the dimensionless units are used in the calculations. Only K_o^* is considered as the fitting parameter, since the area density of the adsorption site n^* depends on the geometry of the solid surface which does not change during the simulation. The assumption of $n^* = 1/\lambda^{*2}$ is adopted, and it is reasonable to assume that $n^* = 2/(l_c^{*2}) = 2.62$ as the surface density of FCC structure, where $l_c^* = 0.8737$ is the lattice constant of the solid. Hence, K_o^* is calculated by fitting Eq. (17) against the simulation results and listed in Table 4 as $K_{o,fit}^*$. The fitted curves of $(\cos\theta_s - \cos\theta)$ against v are plotted in Fig. 9b. Theoretically, one can use Eq. (21) to calculate K_o^* as well, given $V_l^* = 1/\rho_{water}^*$, the viscosity of water η_{water}^*, the interfacial tension between water and CO_2 γ^*, and the static contact angle θ_s. The calculated K_o^* is also reported as $K_{o,cal}^*$ in Table 4.

The effect of the simulated static contact angle θ_s on the calculated jump frequency $K_{o,cal}^*$ is much higher than that on the fitted jump frequency $K_{o,fit}^*$, which suggests that K_o^* may not be estimated correctly using Eq. (21). One possible reason is the assumption that Δg_s^* is approximately equal to W_a^* [Eq. (20)], which is not correct for our simulated system. Δg_s^* can be estimated from Eq. (19) with $K_{o,fit}^*$ from the simulation and is compared with $W_a^* = \gamma^*(1 + \cos\theta_{l,s})$ in Table 4 as well. It can be seen from Table 4 that $\Delta g_s^* < W_a^*$ for all the cases. The previous molecular dynamic simulation of Lennard–Jones polymers for a liquid–vapour–solid system suggested that Δg_s^* is similar to W_a^* [62, 63], but it is not the case for our simulated CO_2–water–silica system. It was

Table 4 The values of the fitted jump frequency $K_{o,fit}^*$, calculated jump frequency $K_{o,cal}^*$, Δg_s^* and $W_a^* = \gamma^*(1 + \cos\theta_{l,s})$ at different silica–water interaction energy ε_{sw}^*

ε_{sw}^*	$\theta_{l,s}$ (°)	$K_{o,fit}^*$	$K_{o,cal}^*$	Δg_s^*	W_a^*
0.5	30.54	0.0293	0.0029	6.893	12.97
0.45	47.88	0.0397	0.0048	6.098	11.64
0.4	62.51	0.0376	0.0084	6.245	10.18
0.3	83.96	0.0529	0.0216	5.348	7.699

$K_{o,fit}^*$ is estimated by fitting Eq. (17) to the simulation results, and Δg_s^* is calculated using $K_{o,fit}^*$ from Eq. (19). $K_{o,cal}^*$ is estimated using Eq. (21) for the simulations with different ε_{sw}^*

also mentioned in [60] that the assumption of Δg_s^* similar to W_a^* only provides the qualitative relationship between the dynamic contact angle and the contact line velocity. Besides, although both Δg_s^* and W_a^* decrease with the decrease of ε_{sw}^* the rate of decrease of Δg_s^* is smaller than that of W_a^*. It could be possible that the simulated silica surface is still highly water-wet (in the water–vapour–silica system) even though ε_{sw}^* has been decreased, and hence there is a limited effect of varying ε_{sw}^* on Δg_s^*. However, more work should be carried out to test this hypothesis.

The static contact angle can also be adjusted by changing the interaction energy between CO_2 and silica, and the corresponding dynamic contact angle results against v are shown in Fig. 10a. It is found that the change in the interaction energy between CO_2 and silica does not have a significant effect on the relationship between ($\cos\theta_s - \cos\theta$) versus v, as shown in Fig. 10b. A possible reason could be that Δg_s^* counts the contribution of the solid–liquid interactions but does not count the solid–gas interactions, suggesting that the effect of the liquid–gas interactions is minor, even though the static contact angle has been changed significantly. In addition, the viscosity of the CO_2 is relatively low compared to the viscosity of water, and hence CO_2 contributes less resistance than the water at the three-phase contact line. These results may further suggest that we cannot simply assume Δg_s^* is similar to W_a^* [Eq. (20)] when the static contact angle is varied due to the variation of gas–solid interactions for our simulated CO_2–water–silica systems.

4 Summary and conclusion

A CGMD framework for the modelling of CO_2/water flows in silica at the micrometer length scales and microsecond time scales is presented, which can be used to study the dynamic behaviour of the multiphase systems. Much greater length and time scales can be achieved by the proposed CGMD method than MD. The conventional MD method can study the dynamic wetting phenomena for the channel with a length scale of nanometers (1–10 nm) at a time scale of ~ 10 ns, while we demonstrate that the CGMD method can handle ~ 1 μm channels at a time scale of ~ 1 microseconds, with a relatively high fidelity that reproduces dynamic wetting phenomena with much shorter computational time.

After the calibration of the inter-particle interactions for the systems, it has been shown that the density and viscosity of CO_2 and water, the interfacial tension between CO_2 and water, and the wettability of the simulated CO_2–water–silica system can be recovered for a wide range of pressure. The dynamic contact angles have been calculated at the different contact line velocities and capillary numbers under three different pressures, but there is no obvious pressure dependence of the dynamic contact angle. The dynamic contact angle results are analysed using the MKT equations by adjusting the silica–water and silica–CO_2 interactions. It is found that the specific activation free energy of wetting per unit area from the liquid–solid interaction Δg_s^* is smaller than the reversible work of adhesion between liquid and solid W_a^*. Furthermore, the silica–CO_2 interaction does not affect how ($\cos\theta_s - \cos\theta$) changes with v, although it can affect the static contact angles. These results suggest that the assumption of Δg_s^* similar to W_a^* in the framework of MKT may not hold for our simulated CO_2–water–silica systems, with highly water-wet silica surface when there is no CO_2 phase. Further investigations should be carried out to study the phenomena.

With further developments, the CGMD method can be a powerful tool to study multiphase interaction problems for the gas–liquid–solid system at the microscale. For example, it can be used to study the dynamic wetting in multiple micropores. It is possible to add more features to the current framework to study more complicated problems in the future, such as modelling the flow behaviour at the solid surface with roughness and the deformation and fracture of the solid due to high fluid pressure.

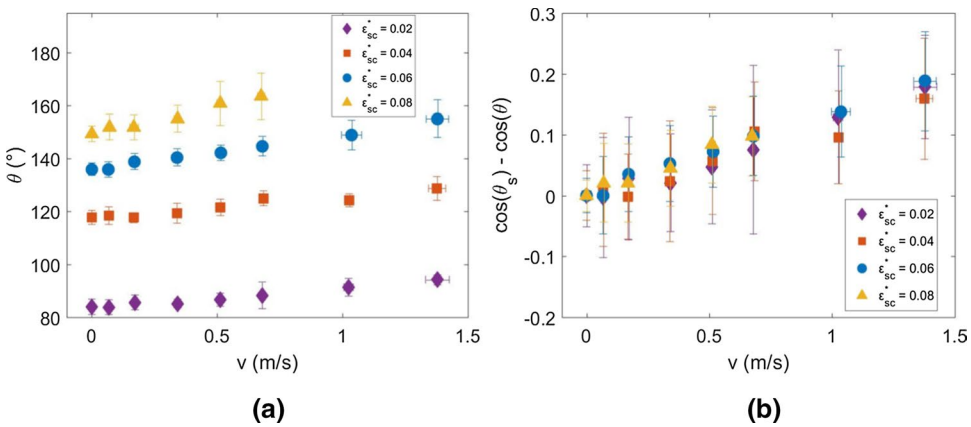

Fig. 10 **a** CO_2 contact angle against the contact line velocity, and **b** the difference between cosines of the static and dynamic contact angles against the contact line velocity with different static contact angles by changing the interactions between CO_2 and solid particles

Acknowledgements This work was supported in part by the Australian Research Council through Discovery Projects (DP170102886 and DP190102954). P.H. acknowledges the financial support from The University of Sydney Nano Institute Postgraduate Top-Up Scholarship. This research was undertaken and supported with the assistance of resources and services from the National Computational Infrastructure (NCI), which is supported by the Australian Government, and the University of Sydney HPC service at The University of Sydney.

Appendices

Appendix 1: Calculation of density

The calculations of density at different pressures for MDPD and DPD particles follow a procedure similar to our previous work [37]. 8000 particles are created in a cubic simulation box with periodic boundary conditions in all three directions. The system is run in the *NPT* ensemble at a constant temperature T^* and pressure P^* for 100,000 time steps. The instantaneous density is calculated at every 20 time steps. The average density and the standard deviation are calculated from the instantaneous density obtained from the last 50,000 time steps. A time step $\Delta t^* = 0.0025$ is used.

Appendix 2: Calculation of viscosity

For the calculation of viscosity at a particular pressure, a system composed of 3000 particles (MDPD or DPD) is created in a periodic simulation box with a particle density calculated at the studied pressure. The aspect ratio of the simulation box is $L_x^*:L_y^*:L_z^* = 1:1:3$. The system is first equilibrated with a Langevin thermostat for 100,000 time steps. The Müller-Plathe algorithm is then applied to calculate the viscosity [64]. A schematic diagram of the simulated system is shown in Fig. 11. The system is divided into 20 layers in the z-direction. At every 50 time steps, the particle in the first layer with the largest speed in the positive x-direction is selected. Similarly, the particle in the middle layer (11th layer) with the largest speed in the negative x-direction is selected. The x-components of the momenta of the two particles are then exchanged. The exchange of momenta induces a shear velocity profile in the system with periodic boundary conditions. The simulations are run for 1,100,000 time steps at the *NVT* ensemble using the Nosé–Hoover chains thermostat. The first 100,000 time steps are considered as the equilibrium run, for the development of the velocity profile. The last 1,000,000 time steps are considered as the production run. The velocity profile is calculated at every 10,000 time steps by averaging the x-component of the particle velocities in each layer. The total momentum exchanged p_x^* is calculated at every 10,000 time steps. In the steady state, the momentum flux J^* can be calculated as:

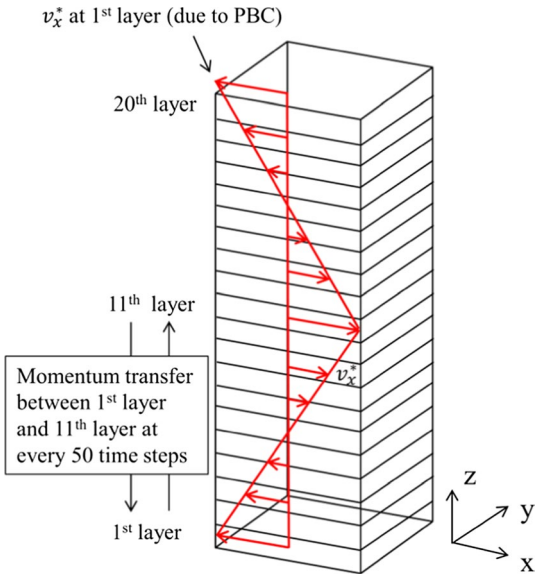

Fig. 11 A schematic diagram of the simulated system for the calculation of viscosity using the Müller–Plathe algorithm [64]. The x-component velocity profile is plotted in red colour. (Color figure online)

$$J^* = p_x^*/2t^*L_x^*L_y^*, \tag{22}$$

where t^* is the time duration of the production run; L_x^* and L_y^* are the length of the simulation box in the x- and y-directions, respectively. The factor of 2 is used here due to the periodic boundary conditions applied. Therefore, the viscosity η^* can be calculated by:

$$J^* = -\eta^* \frac{\partial v_x^*}{\partial z^*}, \tag{23}$$

where $\partial v_x^*/\partial z^*$ is the gradient of the x-component of the fluid velocity with respect to the z-direction within the region between the first and middle layers. The averaged viscosity can be calculated using Eqs. (22) and (23) from the production run. The value of J^* is obtained at the end of the simulation. $\partial v_x^*/\partial z^*$ is calculated from the slope of the time-averaged velocity profile by linear regression at every 10,000 time steps. The average of $\partial v_x^*/\partial z^*$ is then calculated from the 100 samples of the slope. The simulations are repeated five times for each case, and the average and standard deviation of the viscosity are then calculated accordingly.

Appendix 3: Calculation of interfacial tension

The CO_2–water interface simulation is performed to calculate the interfacial tension of the CO_2–water system at a certain T^* and P^*. To construct the system, an 8000-water-particle cubic box, which is equilibrated at targeted T^* and P^* with periodic boundary conditions applied in all three

dimensions, is prepared. The CO_2 box is also prepared with the same size as the water box. The particle numbers of CO_2 in the box is calculated from the equilibrium density at the targeted T^* and P^*. The two boxes are replicated twice in the z-direction and placed together in a periodic simulation box with a ratio of $L_x^*:L_y^*:L_z^* = 1:1:4$. An energy minimization process is applied to the system at the beginning to avoid the particle overlapping at the two CO_2–water interfaces. The water phase is first relaxed by allowing the water particles to move at the Langevin thermostat for 10,000 time steps, while the CO_2 particles are fixed. The CO_2 phase is then relaxed at the Langevin thermostat with water particles being fixed for 10,000 time steps. Next, the whole system is relaxed together at the Langevin thermostat for another 10,000 time steps. An example of a relaxed system is shown in Fig. 12. The relaxed system is then further equilibrated under the NP_zT ensemble for 100,000 time steps to reach the targeted T^* and P^*. The system is then switched to the NVT ensemble and run for 1,000,000 time steps. The last 600,000 time steps are considered as the production run. The interfacial tension γ^* is calculated as:

$$\gamma^* = \frac{1}{2}L_z^*\left\langle P_{zz}^* - \frac{P_{xx}^* + P_{yy}^*}{2}\right\rangle, \tag{24}$$

where P_{xx}^*, P_{yy}^*, and P_{zz}^* are the x-, y-, and z-components of the virial pressure of the system; L_z^* is the length of the simulation box in the z-direction; the time averages are performed inside of $<>$ for the data recorded every 20 time steps. The statistical errors of the surface tension are estimated by calculating the statistical inefficiency [42, 65, 66].

Appendix 4: Water bridge simulation

A liquid bridge simulation is performed to ensure that the selected parameters of water–silica interactions would be able to generate a complete wetting of the silica surface. A periodic simulation box with $L_x^* = 50.67$, $L_y^* = 10.48$, and $L_z^* = 26.38$ is created with water sandwiched between two silica slabs. The particle density of water is initially close to the bulk water density of the equilibrium water–vapour system. The water particles are equilibrated at the Langevin thermostat for 100,000 time steps, with the fixed solid particles. Next, the left and right portions of the water particles are deleted with around one-third of the water particles remaining in the middle between the two silica slabs. Figure 13 shows a snapshot of the initial state of the remained water particles between the two silica slabs. The system is further equilibrated under the NVT ensemble with a Nosé–Hoover chains thermostat until it reaches equilibrium. If the water particles spread over and cover all the silica surfaces inside, it indicates a complete wetting of the simulated silica surface.

Appendix 5: Contact angle measurements

There are different ways of measuring contact angles. In this work, the contact angle is measured by fitting a circle to the interface by assuming a circular shape of the interface. The simulation box is divided into small square bins with a size of $0.5r_c \times 0.5r_c$ (equivalent to 0.01768×0.01768 μm^2) in the x–z plane, and the time-averaged density in each bin is calculated at every 100,000 time steps throughout the simulations, with instantaneous density recorded every 20 time steps. For the simulations with the piston moving at a large velocity greater than 0.7 m/s, the 2D density profile is calculated at every 10,000 time steps and the movement of the piston in the x-axis is also checked at every 10,000 time steps. When the piston has moved one bin width forward ($0.5r_c$), the calculated density profile should be shifted one bin width backward in order to have a stable water–CO_2 interface at large piston velocity. In addition, the first bin at the x-direction should be moved to the end due to the periodic boundary condition applied along the x-axis. Hence, the shifted density profiles are averaged again to obtain the

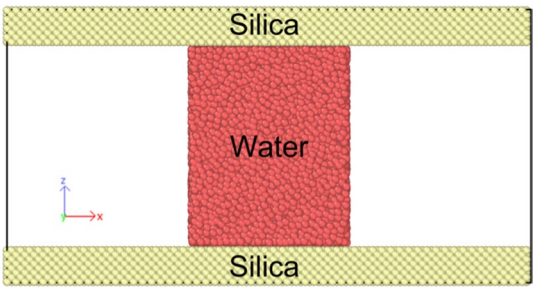

Fig. 13 A snapshot of the initial state of the system for the liquid bridge simulation

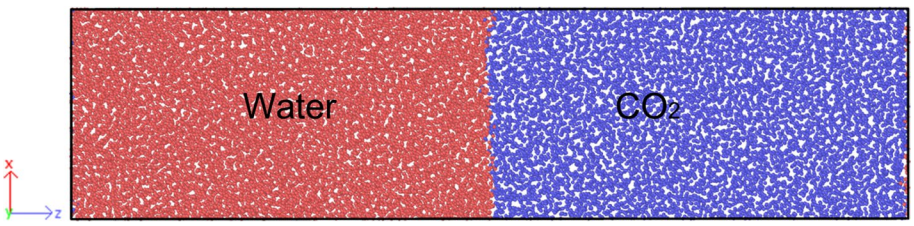

Fig. 12 A snapshot of the system of the water–CO_2 interface simulation after being relaxed at the Langevin thermostat

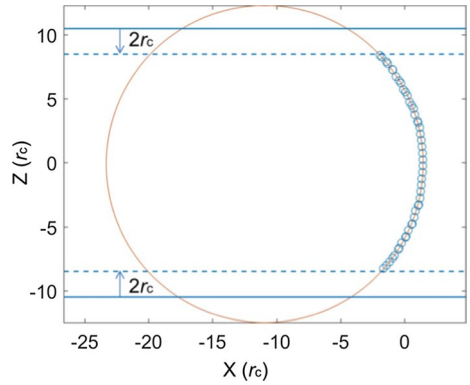

Fig. 14 The measurement of the contact angle by fitting a circle to the interface. The markers of small circles are the coordinates of the water–CO_2 interfaces. The solid blue lines indicate the location of the solid surface, and the interface data between the two blue dashed lines are used in the circle fitting

density profile at every 100,000 time steps, in order to calculate the contact angle. The 2D density contour is plotted using Matlab. The location of the interface between CO_2 and water can be calculated from the 2D density contour by calculating the density at the interface $\rho_{\text{int}} = 0.5(\rho_{\text{water}} + \rho_{\text{CO2}})$, where ρ_{water} and ρ_{CO2} are the bulk densities of water and CO_2, respectively, which can be estimated from the bulk regions in water and CO_2 phases. Since the density perturbations can happen near the solid surface, only the interface data that are $2r_c$ away from the solid surface are used to fit the circle. An example of the circular fitting is shown in Fig. 14. The contact angle is calculated from the tangent of the circle where the circle and solid surfaces meet. The contact angle values are calculated by averaging all the top and bottom contact angles during the production run, and the standard deviations of the contact angles are calculated accordingly.

References

1. Chukwudeme E, Hamouda A (2009) Enhanced oil recovery (EOR) by miscible CO2 and water flooding of asphaltenic and non-asphaltenic oils. Energies 2(3):714–737
2. Middleton RS, Carey JW, Currier RP, Hyman JD, Kang Q, Karra S, Jiménez-Martínez J, Porter ML, Viswanathan HS (2015) Shale gas and non-aqueous fracturing fluids: opportunities and challenges for supercritical CO2. Appl Energy 147:500–509
3. Koh DY, Kang H, Kim DO, Park J, Cha M, Lee H (2012) Recovery of methane from gas hydrates intercalated within natural sediments using CO_2 and a CO_2/N_2 gas mixture. Chemsuschem 5(8):1443–1448
4. Jung J-W, Wan J (2012) Supercritical CO_2 and ionic strength effects on wettability of silica surfaces: equilibrium contact angle measurements. Energy Fuels 26(9):6053–6059
5. Sarmadivaleh M, Al-Yaseri AZ, Iglauer S (2015) Influence of temperature and pressure on quartz–water–CO_2 contact angle and CO_2–water interfacial tension. J Colloid Interface Sci 441:59–64
6. Espinoza DN, Santamarina JC (2010) Water–CO_2–mineral systems: interfacial tension, contact angle, and diffusion—implications to CO_2 geological storage. Water Resour Res 46(7):W07537
7. Chen C, Dong B, Zhang N, Li W, Song Y (2016) Pressure and temperature dependence of contact angles for CO_2/water/silica systems predicted by molecular dynamics simulations. Energy Fuels 30(6):5027–5034
8. Iglauer S, Mathew M, Bresme F (2012) Molecular dynamics computations of brine–CO_2 interfacial tensions and brine–CO_2–quartz contact angles and their effects on structural and residual trapping mechanisms in carbon geo-sequestration. J Colloid Interface Sci 386(1):405–414
9. Javanbakht G, Sedghi M, Welch W, Goual L (2015) Molecular dynamics simulations of CO_2/water/quartz interfacial properties: impact of CO_2 dissolution in water. Langmuir 31(21):5812–5819
10. Chen C, Zhang N, Li W, Song Y (2015) Water contact angle dependence with hydroxyl functional groups on silica surfaces under CO_2 sequestration conditions. Environ Sci Technol 49(24):14680–14687
11. Iglauer S, Salamah A, Sarmadivaleh M, Liu K, Phan C (2014) Contamination of silica surfaces: impact on water–CO_2–quartz and glass contact angle measurements. Int J Greenhouse Gas Control 22:325–328
12. Huang P, Shen L, Gan Y, Maggi F, El-Zein A, Pan Z (2019) Atomistic study of dynamic contact angles in CO_2–water–silica system. Langmuir 35(15):5324–5332
13. Friedman SP (1999) Dynamic contact angle explanation of flow rate-dependent saturation–pressure relationships during transient liquid flow in unsaturated porous media. J Adhes Sci Technol 13(12):1495–1518
14. Liu H, Ju Y, Wang N, Xi G, Zhang Y (2015) Lattice Boltzmann modeling of contact angle and its hysteresis in two-phase flow with large viscosity difference. Phys Rev E 92(3):033306
15. Li L, Shen L, Nguyen GD, El-Zein A, Maggi F (2018) A smoothed particle hydrodynamics framework for modelling multiphase interactions at meso-scale. Comput Mech 62(5):1071–1085
16. Bao Y, Li L, Shen L, Lei C, Gan Y (2019) Modified smoothed particle hydrodynamics approach for modelling dynamic contact angle hysteresis. Acta Mech Sin 35(3):472–485
17. Shadloo M, Zainali A, Yildiz M (2013) Simulation of single mode Rayleigh–Taylor instability by SPH method. Comput Mech 51(5):699–715
18. Saha AA, Mitra SK (2009) Effect of dynamic contact angle in a volume of fluid (VOF) model for a microfluidic capillary flow. J Colloid Interface Sci 339(2):461–480
19. Li S, Fan H (2015) On multiscale moving contact line theory. Proc R Soc A 471(2179):20150224
20. Minaki H, Li S (2014) Multiscale modeling and simulation of dynamic wetting. Comput Methods Appl Mech Eng 273:273–302
21. Cook BK, Noble DR, Williams JR (2004) A direct simulation method for particle-fluid systems. Eng Comput 21(2–4):151–168
22. Jing L, Kwok C, Leung Y, Sobral Y (2016) Extended CFD–DEM for free-surface flow with multi-size granules. Int J Numer Anal Methods Geomech 40(1):62–79
23. Das R, Cleary PW (2015) Evaluation of accuracy and stability of the classical SPH method under uniaxial compression. J Sci Comput 64(3):858–897
24. Avendano C, Lafitte T, Galindo A, Adjiman CS, Jackson G, Müller EA (2011) SAFT-γ force field for the simulation of molecular fluids. 1. A single-site coarse grained model of carbon dioxide. J Phys Chem B 115(38):11154–11169
25. Lobanova O, Avendaño C, Lafitte T, Müller EA, Jackson G (2015) SAFT-γ force field for the simulation of molecular fluids: 4. A

single-site coarse-grained model of water applicable over a wide temperature range. Mol Phys 113(9–10):1228–1249
26. Marrink SJ, De Vries AH, Mark AE (2004) Coarse grained model for semiquantitative lipid simulations. J Phys Chem B 108(2):750–760
27. Chiu S-W, Scott HL, Jakobsson E (2010) A coarse-grained model based on Morse potential for water and n-alkanes. J Chem Theory Comput 6(3):851–863
28. Groot RD, Warren PB (1997) Dissipative particle dynamics: bridging the gap between atomistic and mesoscopic simulation. J Chem Phys 107(11):4423–4435
29. Warren P (2003) Vapor–liquid coexistence in many-body dissipative particle dynamics. Phys Rev E 68(6):066702
30. Pagonabarraga I, Frenkel D (2001) Dissipative particle dynamics for interacting systems. J Chem Phys 115(11):5015–5026
31. Arienti M, Pan W, Li X, Karniadakis G (2011) Many-body dissipative particle dynamics simulation of liquid/vapor and liquid/solid interactions. J Chem Phys 134(20):204114
32. Kumar A, Asako Y, Abu-Nada E, Krafczyk M, Faghri M (2009) From dissipative particle dynamics scales to physical scales: a coarse-graining study for water flow in microchannel. Microfluid Nanofluidics 7(4):467
33. Espanol P, Revenga M (2003) Smoothed dissipative particle dynamics. Phys Rev E 67(2):026705
34. Ellero M, Español P (2018) Everything you always wanted to know about SDPD★(★ but were afraid to ask). Appl Math Mech 39(1):103–124
35. Hu XY, Adams NA (2006) A multi-phase SPH method for macroscopic and mesoscopic flows. J Comput Phys 213(2):844–861
36. Lei H, Baker NA, Wu L, Schenter GK, Mundy CJ, Tartakovsky AM (2016) Smoothed dissipative particle dynamics model for mesoscopic multiphase flows in the presence of thermal fluctuations. Phys Rev E 94(2):023304
37. Huang P, Shen L, Gan Y, Nguyen GD, El-Zein A, Maggi F (2018) Coarse-grained modeling of multiphase interactions at microscale. J Chem Phys 149(12):124505
38. Ruckenstein E, Liu H (1997) Self-diffusion in gases and liquids. Ind Eng Chem Res 36(9):3927–3936
39. Liu H, Silva CM, Macedo EA (1997) New equations for tracer diffusion coefficients of solutes in supercritical and liquid solvents based on the Lennard–Jones fluid model. Ind Eng Chem Res 36(1):246–252
40. Lemmon EW, McLinden MO, Friend DG. Thermophysical properties of fluid systems. In: Linstrom PJ, Mallard WG (eds) NIST Chemistry WebBook, NIST Standard Reference Database Number 69. National Institute of Standards and Technology, Gaithersburg MD, 20899. https://doi.org/10.18434/t4d303
41. Shinoda W, Shiga M, Mikami M (2004) Rapid estimation of elastic constants by molecular dynamics simulation under constant stress. Phys Rev B 69(13):134103
42. Allen MP, Tildesley DJ (1987) Computer simulation of liquids. Oxford University Press, New York
43. Georgiadis A, Maitland G, Trusler JM, Bismarck A (2010) Interfacial tension measurements of the ($H_2O + CO_2$) system at elevated pressures and temperatures. J Chem Eng Data 55(10):4168–4175
44. Groot RD, Rabone K (2001) Mesoscopic simulation of cell membrane damage, morphology change and rupture by nonionic surfactants. Biophys J 81(2):725–736
45. Ghoufi A, Malfreyt P (2011) Mesoscale modeling of the water liquid–vapor interface: a surface tension calculation. Phys Rev E 83(5):051601
46. Farokhpoor R, Bjørkvik BJ, Lindeberg E, Torsæter O (2013) Wettability behaviour of CO_2 at storage conditions. Int J Greenhouse Gas Control 12:18–25
47. Li X, Fan X (2015) Effect of CO2 phase on contact angle in oil-wet and water-wet pores. Int J Greenhouse Gas Control 36:106–113
48. Plimpton S (1995) Fast parallel algorithms for short-range molecular dynamics. J Comput Phys 117(1):1–19
49. Rushton M (2014) atsim.potentials. http://atsimpotentials.readthedocs.io/en/latest/. Accessed 14 Apr 2016
50. Frenkel D, Smit B (2001) Understanding molecular simulation: from algorithms to applications, vol 1. Academic Press, San Diego
51. Martyna GJ, Tobias DJ, Klein ML (1994) Constant pressure molecular dynamics algorithms. J Chem Phys 101(5):4177–4189
52. Stukowski A (2009) Visualization and analysis of atomistic simulation data with OVITO—the Open Visualization Tool. Modell Simul Mater Sci Eng 18(1):015012
53. Li X, Fan X, Askounis A, Wu K, Sefiane K, Koutsos V (2013) An experimental study on dynamic pore wettability. Chem Eng Sci 104:988–997
54. Jiang T-S, Soo-Gun O, Slattery JC (1979) Correlation for dynamic contact angle. J Colloid Interface Sci 69(1):74–77
55. Bachu S, Bennion DB (2008) Interfacial tension between CO_2, freshwater, and brine in the range of pressure from (2 to 27) MPa, temperature from (20 to 125) °C, and water salinity from (0 to 334 000) mg L − 1. J Chem Eng Data 54(3):765–775
56. Bikkina PK, Shoham O, Uppaluri R (2011) Equilibrated interfacial tension data of the CO_2–water system at high pressures and moderate temperatures. J Chem Eng Data 56(10):3725–3733
57. Bikkina PK (2011) Contact angle measurements of CO_2–water–quartz/calcite systems in the perspective of carbon sequestration. Int J Greenhouse Gas Control 5(5):1259–1271
58. Rohatgi A WebPlotDigitizer, Version 4.1. https://automeris.io/WebPlotDigitizer. Accessed Jan 2018
59. Blake T, Haynes J (1969) Kinetics of liquid–liquid displacement. J Colloid Interface Sci 30(3):421–423
60. Blake T, De Coninck J (2002) The influence of solid–liquid interactions on dynamic wetting. Adv Colloid Interface Sci 96(1–3):21–36
61. Glasstone S, Laidler K, Eyring H (1941) The theory of rate processes. McGraw-Hill Book Co. Inc., New York
62. Bertrand E, Blake TD, De Coninck J (2009) Influence of solid–liquid interactions on dynamic wetting: a molecular dynamics study. J Phys: Condens Matter 21(46):464124
63. Duvivier D, Blake TD, De Coninck J (2013) Toward a predictive theory of wetting dynamics. Langmuir 29(32):10132–10140
64. Müller-Plathe F (1999) Reversing the perturbation in nonequilibrium molecular dynamics: an easy way to calculate the shear viscosity of fluids. Phys Rev E 59(5):4894
65. Friedberg R, Cameron JE (1970) Test of the Monte Carlo method: fast simulation of a small Ising lattice. J Chem Phys 52(12):6049–6058
66. Fincham D, Quirke N, Tildesley D (1986) Computer simulation of molecular liquid mixtures. I. A diatomic Lennard-Jones model mixture for CO_2/C_2H_6. J Chem Phys 84(8):4535–4546